

# Full-range birefringence control with piezoelectric MEMS-based metasurfaces

**Chao Meng**

Center for Nano Optics, University of Southern Denmark

**Paul Thrane**

Center for Nano Optics, University of Southern Denmark

**Fei Ding**

University of Southern Denmark <https://orcid.org/0000-0001-7362-519X>

**Sergey Bozhevolnyi** (✉ [seib@mci.sdu.dk](mailto:seib@mci.sdu.dk))

Center for Nano Optics, University of Southern Denmark <https://orcid.org/0000-0002-0393-4859>

---

## Research Article

### Keywords:

**Posted Date:** December 3rd, 2021

**DOI:** <https://doi.org/10.21203/rs.3.rs-1137478/v1>

**License:** © ⓘ This work is licensed under a Creative Commons Attribution 4.0 International License.

[Read Full License](#)

---

# **Full-range birefringence control with piezoelectric MEMS-based metasurfaces**

Chao Meng,<sup>1†</sup> Paul C. V. Thrane,<sup>1,2†</sup> Fei Ding,<sup>1\*</sup> and Sergey I. Bozhevolnyi<sup>1\*</sup>

<sup>1</sup>*Centre for Nano Optics, University of Southern Denmark, Campusvej 55, Odense DK-5230, Denmark*

<sup>2</sup>*SINTEF Microsystems and Nanotechnology, Gaustadalleen 23C, 0737 Oslo, Norway*

†These authors contributed equally to this work

\*Corresponding author emails: feid@mci.sdu.dk (F.D.); seib@mci.sdu.dk (S.I.B.)

**Dynamic polarization control is crucial for emerging highly integrated photonic systems with diverse metasurfaces being explored for its realization<sup>1-6</sup>, but efficient, fast, and broadband operation remains a cumbersome challenge. While efficient optical metasurfaces (OMSs) involving liquid crystals suffer from inherently slow responses<sup>1</sup>, other OMS realizations are limited either in the operating wavelength range (due to resonances involved)<sup>2,3</sup> or in the range of birefringence tuning<sup>4-6</sup>.**

**Capitalizing on our development of piezoelectric micro-electro-mechanical system (MEMS) based dynamic OMSs<sup>7</sup>, we demonstrate reflective MEMS-OMS dynamic wave plates (DWPs) with high polarization conversion efficiencies (~ 75%), broadband operation (~ 100 nm near the operating wavelength of 800 nm), fast responses (< 0.4 milliseconds) and full-range birefringence control that enables completely encircling the Poincaré sphere along trajectories determined by the incident light polarization and DWP orientation. Demonstrated complete electrical control over light polarization opens new avenues in further integration and miniaturization of optical networks and systems<sup>8,9</sup>.**

Recent years brought explosive growth of OMS applications in terms of both diversity and sophistication<sup>10</sup>, especially with OMS configurations becoming dynamic, i.e., offering not only spatial but also temporal control over transmitted and reflected optical fields<sup>11</sup>. Plentiful dynamic OMSs have been demonstrated in the past decade, implementing active *amplitude* and *phase* modulation with diversified functionalities<sup>12-19</sup>. Despite significant progress achieved in dynamic control of amplitude and phase responses, OMS-enabled active *polarization* control in the optical range remains largely unexplored. At the same time, the polarization of light is crucial for realization of adaptive integrated photonic systems due to the fundamental role of polarization as another intrinsic characteristic of optical waves, which is uncorrelated with the amplitude and phase. To implement active polarization control with dynamic OMSs, one should be able of dynamically tuning the OMS optical anisotropy in a wide range. The corresponding OMS realizations rely on the birefringence property of natural materials<sup>1,2</sup> or metasurfaces<sup>3-6,20,21</sup>, consisting of anisotropic meta-atoms. In either case, since available OMS thickness (i.e., interaction length) and birefringence are limited, identification of a suitable OMS configuration is a rather complicated and arduous issue, with the outcome

exhibiting drawbacks, such as slow responses, narrow bandwidths, limited dynamic ranges of birefringence, and low polarization conversion efficiencies (Supplementary Table 1).

In this Letter, we demonstrate electrically controlled full-range birefringence by integrating a plasmonic OMS with judiciously designed anisotropic meta-atoms and a thin-film piezoelectric MEMS mirror. The resulting MEMS-OMS-based DWP operates in reflection, featuring continuously varied anisotropy and enabling complete encircling of the Poincaré sphere, e.g., the polarization conversion from linear to circular, orthogonal linear and opposite circular polarizations (Fig. 1). The OMS component, which is composed of a glass substrate with an OMS layer containing a 2D array of identical rectangular gold nanobricks, is placed close to an actuated MEMS gold mirror, whose separation  $T_a$  from the OMS is accurately controlled by applying the actuation voltage  $V_m$  (Fig. 1a). In the conceptual schematic, a linearly polarized (LP) light beam is incident onto the DWP, and the polarization state of the reflected light is shown continuously adjusted by changing the actuation voltage, with different polarization trajectories encircling the Poincaré sphere being available for different DWP orientations (Fig. 1a).

Variable birefringence of the proposed DWP originates from the anisotropy of OMS elements placed at different distances from the MEMS mirror<sup>7</sup>, and can be described by considering the hybrid OMS-integrated Fabry–Pérot (FP) configuration<sup>22–24</sup>. For example, large reflectivities along with large phase differences ( $> 270^\circ$ ) for two orthogonal linear polarizations can be realized for the operation wavelength  $\lambda = 800$  nm at a specific air gap of  $T_a = 400$  nm for OMS nanobricks with sufficiently large aspect ratios (Fig. 1b). By varying the gap  $T_a$ , the phase difference, i.e., the DWP birefringence, can be dramatically changed, covering the whole tuning range of  $0-2\pi$ , in a periodic fashion with the spatial period  $\lambda/2 = 400$  nm (Fig. 1c). Note that the selected size of the OMS unit cell is  $A = 250$  nm ( $A < \lambda/2$ ), resulting in our choice of the nanobrick long side length  $L_u = 200$  nm due to the electron-beam lithography (EBL) fabrication (aspect ratio) constraints. The short side length  $L_v$  is determined by maximizing reflection amplitudes for both orthogonal polarizations (i.e.,  $|r_{uu}|$  and  $|r_{vv}|$ ) expected at all air gaps  $T_a$  along with ensuring the full-range birefringence control (Fig. 1c and Complementary Fig. S1). The nanobrick height is also optimized to enable the full-range birefringence control and large reflection amplitudes, resulting in the choice of  $t_m = 50$  nm, a value that conforms well with

the fabrication tolerances (Supplementary Fig. S1). Variations in the reflected field amplitudes ( $|r_{uu}|$ ,  $|r_{vv}|$ ), phases ( $\phi_{uu}$ ,  $\phi_{vv}$ ) and birefringence ( $\Delta\phi_{vu}$ ), when changing the air gap  $T_a$  for the designed DWP unit cell ( $L_u = 200$  nm,  $L_v = 100$  nm), are shown in Fig. 1d, indicating the full  $0-2\pi$  birefringence tunability and large reflection amplitudes ( $> 0.9$ ). Such a distinct polarization-dependent phase response of the designed DWP is achieved due to a very high OMS reflectivity for the light polarized along the long nanobrick side, so that the reflected field phase  $\phi_{uu}$  does not depend on the air gap  $T_a$ , whereas the reflected field phase  $\phi_{vv}$  of the orthogonal polarization varies periodically from 0 to  $2\pi$  with changing the air gap (Supplementary Fig. S2).

Following the simulations and design considerations presented above that indicate the possibility of realizing efficient DWPs with full-range birefringence tunability, we conducted the corresponding experimental investigations. The MEMS-OMS-based DWP for polarization conversion was assembled from a separately fabricated OMS (Fig. 1e) and an ultra-flat MEMS mirror that were wire bonded to a printed circuit board (PCB) for electrical connection (Supplementary Figs. S3 and S4, Methods/Fabrication). Owing to the FP nature of the designed DWP component, the overall response is inherently periodic with respect to the variable air gap  $T_a$ , thus relaxing the requirement for small, nm-sized, air gaps essential for the previously developed MEMS-OMS configurations<sup>7</sup> and thereby simplifying the assembly process. We should however note that the access to nm-sized air gaps, although not easily gained, would allow one to operate the DWP with gap surface plasmons being generated<sup>7</sup>, a regime that promises a slightly broader operation wavelength range as discussed below. To quantify the air gap  $T_a$  at each actuation voltage  $V_m$ , we make use of the air-gap-dependent MEMS-OMS operation<sup>7</sup> by exploiting the fact that the MEMS-OMS behaves as a mirror at periodically distributed air gaps (depending on the light wavelength used) regardless of the OMS design (Supplementary Figs. S5 and S6). By determining the wavelength corresponding to the mirror-like operation (no polarization transformation) at each voltage, it is possible to accurately evaluate *in situ* the air gap  $T_a$  realized in each polarization measurement (Supplementary Fig. S7).

For the characterization of the fabricated DWP performance, a supercontinuum laser beam with the well-defined LP state ( $\theta_{LP} = 90^\circ$ ) was directed onto the DWP oriented at  $\theta_{DWP} = 45^\circ$  (Fig. 2a). The MEMS mirror was electrically actuated to tune the DWP birefringence by changing the MEMS-OMS air gap and thereby

adjust the polarization state of the reflected light. Full Stokes polarimetry<sup>25</sup> was performed by rotating a quarter-wave plate (QWP) and a polarizer, while analyzing the reflected light with a spectrometer (Methods/Characterization, Supplementary Fig. S8). Recording the DWP polarization-resolved reflection spectra (Supplementary Fig. S9) enables the determination of wavelength-resolved Stokes parameters along with the polarization conversion efficiencies and degree of polarization (DOP) while varying the MEMS-OMS air gap (Fig. 2b, Supplementary Figs. S9 and S10). The quality of polarization conversion in the considered configuration and its operation bandwidth can be assessed by requiring efficient modulation of Stokes parameters  $S_1$  and  $S_3$ , while keeping  $S_2$  insignificant. It is seen (Figs. 2b and 2c) that the fabricated DWP performs very good, matching remarkably well the simulations, within  $\sim 100$  nm band (i.e.,  $\sim 10\%$ ) around the design wavelength of  $\lambda = 800$  nm. The experimental polarization conversion efficiencies (for all possible polarization conversions) of the DWP are rather high within the bandwidth (Supplementary Fig. S9), being estimated  $\sim 75\%$  at the design wavelength  $\lambda = 800$  nm (Fig. 2c), due to the full-range birefringence control realized and small absorption losses present in the MEMS-OMS configuration under off-resonance operation. Note that, as the air gap increases, the reflected light polarization changes periodically from incident LP  $|y\rangle$  state to  $|r\rangle$ ,  $|x\rangle$ ,  $|l\rangle$  states (Fig. 2a) with the corresponding Stokes parameters ( $S_1, S_2, S_3$ ) changing from approximately  $(-1, 0, 0)$  to  $(0, 0, 1)$ ,  $(1, 0, 0)$  and  $(0, 0, -1)$ , respectively (Figs. 2b and 2c). This DWP transformation is equivalent to the transformation from the mirror-like operation, or zero-wave plate (ZWP), to QWP, half-wave plate (HWP) and three-quarters-wave plate (TQWP). Note that the DOP remains being close to 1.0 during the whole DWP tuning, indicating an overall purity of polarization conversion. Slight deviations from the ideal conversion can be explained by fabricated nanobrick deviations from the design dimensions, the reflection from the front glass/air interface as well as possible mirror tilting. The polarization trajectory at  $\lambda = 800$  nm follows one complete revolution around the Poincaré sphere, passing through basic polarization states  $|y\rangle$ ,  $|r\rangle$ ,  $|x\rangle$  and  $|l\rangle$ , and circulating repeatedly with increasing  $T_a$  (Fig. 2d, Supplementary Video S1). Note that, in the current experimental demonstration, the DWP is operated with air gaps between 2 and 3  $\mu\text{m}$ , covering two adjacent FP resonance orders and exhibiting practically the same performance.

High contrast between the main orthogonal polarization states ( $|x\rangle$  and  $|y\rangle$ ,  $|r\rangle$  and  $|l\rangle$ ), corresponding to HWP/ZWP and QWP/TQWP transformations, can be visualized at both the direct image (DI) and Fourier image (FI) planes (Fig. 3a, b). The dynamic polarization conversion behavior, induced by actuating the MEMS mirror with alternating voltages at slow switching frequency, is captured by a charge-coupled device (CCD) camera (Supplementary Videos S2 and S3), showing good repeatability and high modulation efficiency. By actuating the MEMS mirror with a periodic rectangular signal, filtering the reflected light with analyzers (i.e.,  $|x\rangle$ ,  $|y\rangle$ ,  $|r\rangle$  or  $|l\rangle$ ) and detecting it with a fast photodetector, we observe relatively fast switching with rise/fall times of  $\sim 0.15/0.11$  ms and  $\sim 0.36/0.23$  ms for respective ZWP/HWP and QWP/TQWP transformations (Fig. 3c, d). The switching time for the QWP/TQWP transformation is  $\sim$  twice longer due to a  $\sim$  twice longer relocation of the MEMS mirror required (Fig. 2c), also reflected in a  $\sim$  twice larger switching voltage used (cf., Figs. 3c and 3d). Note that, by optimizing MEMS mirrors for achieving faster switching, one should be able to reach switching frequencies in the MHz range<sup>15,26</sup>. We should also remark that a baseline voltage of  $\sim 14$  V is used to move the MEMS mirror closer to the OMS, which would not be necessary in devices with more accurate mounting, so that the maximum applied voltage can be kept below  $\sim 6$  V.

In addition to evaluating the DWP polarization tunability, polarization conversion efficiencies, and temporal response, we also explored the possibility of continuous LP rotation by a hybrid QWP-DWP component consisting of a general QWP, whose fast axis is oriented along  $x$  direction, and a DWP oriented at  $\theta_{\text{DWP}} = 45^\circ$  (Fig. 4a, Supplementary Fig. S11). In this configuration, the QWP transforms the LP basis ( $|u\rangle$ ,  $|v\rangle$ ) of the DWP eigenstates into the CP basis ( $|r\rangle$ ,  $|l\rangle$ ) of the hybrid QWP-DWP component, thus enabling continuous LP rotation by tuning the DWP birefringence *via* tuning the air gap  $T_a$ . The reflected light polarization states measured while changing the air gap are visualized by a polarization trajectory around the equator of the Poincaré sphere (Fig. 4a, Supplementary Fig. S11 and Video S4), demonstrating the generation of LP light with arbitrary LP orientation by adjusting the actuation voltage  $V_m$  (i.e., the air gap  $T_a$ ). To ease steering potential practical applications, we have also investigated the polarization transformations realized for different DWP orientations ( $\theta_{\text{DWP}} = 15^\circ, 30^\circ, 60^\circ, 75^\circ$ ) and fixed incident LP state  $|y\rangle$  (Fig. 4b,

Supplementary Fig. S12 and Video S5), as well as for different incident LP states ( $\theta_{LP} = 60^\circ, 75^\circ, 105^\circ, 120^\circ$ ) and fixed DWP orientation  $\theta_{DWP} = 45^\circ$  (Fig. 4c, Supplementary Fig. S13 and Video S6). The polarization trajectories on the Poincaré sphere are seen to be differently tilted for different DWP orientations having the common point, the incident LP state  $|y\rangle$  (Fig. 4b), while being parallel to the plane ( $S_1, S_3$ ) and reflecting the incident LP state (Fig. 4c). Note that, for any given point on the Poincaré sphere, one can identify suitable orientations of the DWP and incident LP state enabling closed polarization trajectories to pass this point, so that a multitude of polarization modulation capabilities can be realized with the same DWP. Finally, we would like to emphasize that *all* experimental results agree exceedingly well with the simulations *without* any fitting parameters, demonstrating convincingly that the fabricated DWP behaves according to the design and that the modelling approach developed is well suited for use in future MEMS-OMS component developments.

To summarize, capitalizing on our development of the MEMS-OMS platform<sup>7</sup> we have demonstrated the electrically driven DWP operating in reflection with high polarization conversion efficiencies ( $\sim 75\%$ ), broadband operation ( $\sim 100$  nm near the operating wavelength of 800 nm), fast responses ( $< 0.4$  ms) and full-range birefringence control that enables completely encircling the Poincaré sphere along trajectories determined by the incident light polarization and DWP orientation. It should be noted that, given the access to nm-sized air gaps, one can exploit the same design principle to realize the DWP with gap surface plasmons being generated<sup>7</sup>, a regime that promises a broader operation wavelength range ( $\sim 160$  nm) although probably at the expense of a lower efficiency ( $\sim 50\%$ )<sup>7</sup>. Importantly, the general approach developed can also be applied to design a DWP operating in transmission by using a partially transmitting MEMS mirror and placing an OMS in the middle of a FP cavity<sup>27</sup>. Given that a multitude of polarization modulation capabilities can be realized with the same DWP, we believe that the demonstrated electrically driven DWP configuration with full-range birefringence control opens fascinating perspectives for successful integration of high-performance compact dynamic polarization components into future miniaturized reconfigurable/adaptive optical systems.

## Competing Interests statement

The paper authors along with Jo Gjessing and Christopher Dirdal from SINTEF are inventors on a related patent application filed by the University of Southern Denmark and SINTEF under United Kingdom Patent Application No. 2113182.6.

## References

1. Yu, P., Li, J. & Liu, N. Electrically tunable optical metasurfaces for dynamic polarization conversion. *Nano Lett.* **21**, 6690–6695 (2021).
2. Biswas, S., Grajower, M. Y., Watanabe, K., Taniguchi, T. & Atwater, H. A. Broadband electro-optic polarization conversion with atomically thin black phosphorus. *Science* **374**, 448–453 (2021).
3. Nicholls, L. H. *et al.* Ultrafast synthesis and switching of light polarization in nonlinear anisotropic metamaterials. *Nat. Photon.* **11**, 628–633 (2017).
4. Schirato, A. *et al.* Transient optical symmetry breaking for ultrafast broadband dichroism in plasmonic metasurfaces. *Nat. Photon.* **14**, 723–727 (2020).
5. Wang, K. *et al.* High contrast, femtosecond light polarization manipulation in epsilon-near-zero material coupled to a plasmonic nanoantenna array. *ACS Photonics* **8**, 2791–2799 (2021).
6. Zanotto, S. *et al.* Optomechanics of chiral dielectric metasurfaces. *Adv. Opt. Mater.* **8**, 1901507 (2020).
7. Meng, C. *et al.* Dynamic piezoelectric MEMS-based optical metasurfaces. *Sci. Adv.* **7**, eabg5639 (2021).
8. Dai, D., Bauters, J. & Bowers, J. E. Passive technologies for future large-scale photonic integrated circuits on silicon: Polarization handling, light non-reciprocity and loss reduction. *Light Sci. Appl.* **1**, e1 (2012).
9. He, C. *et al.* Polarisation optics for biomedical and clinical applications: a review. *Light Sci. Appl.* **10**, 194 (2021).
10. Ding, F., Pors, A. & Bozhevolnyi, S. I. Gradient metasurfaces: A review of fundamentals and applications. *Reports Prog. Phys.* **81**, 026401 (2018).
11. Shaltout, A. M., Shalaev, V. M. & Brongersma, M. L. Spatiotemporal light control with active metasurfaces. *Science* **364**, eaat3100 (2019).
12. Wang, Q. *et al.* Optically reconfigurable metasurfaces and photonic devices based on phase change materials. *Nat. Photon.* **10**, 60–65 (2016).
13. Li, S. Q. *et al.* Phase-only transmissive spatial light modulator based on tunable dielectric metasurface. *Science* **364**, 1087–1090 (2019).
14. Wu, P. C. *et al.* Dynamic beam steering with all-dielectric electro-optic III–V multiple-quantum-well metasurfaces. *Nat. Commun.* **10**, 3654 (2019).
15. Holsteen, A. L., Cihan, A. F. & Brongersma, M. L. Temporal color mixing and dynamic beam shaping with silicon metasurfaces. *Science* **365**, 257–260 (2019).

16. van de Groep, J. *et al.* Exciton resonance tuning of an atomically thin lens. *Nat. Photon.* **14**, 426–430 (2020).
17. Shalaginov, M. Y. *et al.* Reconfigurable all-dielectric metalens with diffraction-limited performance. *Nat. Commun.* **12**, 1225 (2021).
18. Zhang, Y. *et al.* Electrically reconfigurable non-volatile metasurface using low-loss optical phase-change material. *Nat. Nanotechnol.* **16**, 661–666 (2021).
19. Wang, Y. *et al.* Electrical tuning of phase-change antennas and metasurfaces. *Nat. Nanotechnol.* **16**, 667–672 (2021).
20. Shi, Z. *et al.* Continuous angle-tunable birefringence with freeform metasurfaces for arbitrary polarization conversion. *Sci. Adv.* **6**, eaba3367 (2020).
21. Zhang, X. *et al.* Controlling angular dispersions in optical metasurfaces. *Light Sci. Appl.* **9**, 76 (2020).
22. Chen, H.-T. Interference theory of metamaterial perfect absorbers. *Opt. Express* **20**, 7165 (2012).
23. Ameling, R. & Giessen, H. Microcavity plasmonics: Strong coupling of photonic cavities and plasmons. *Laser Photon. Rev.* **7**, 141–169 (2013).
24. Berkhout, A. & Koenderink, A. F. Perfect absorption and phase singularities in plasmon antenna array etalons. *ACS Photonics* **6**, 2917–2925 (2019).
25. Goldstein, D. H. *Polarized Light*. (Taylor and Francis, 2010).
26. Wang, T., Sawada, R. & Lee, C. A piezoelectric micromachined ultrasonic transducer using piston-like membrane motion. *IEEE Electron Device Lett.* **36**, 957–959 (2015).
27. Berkhout, A., Wolterink, T. A. W. & Koenderink, A. F. Strong coupling to generate complex birefringence: metasurface in the middle etalons. *ACS Photonics* **7**, 2799–2806 (2020).
28. Johnson, P. B. & Christy, R. W. Optical constants of the noble metals. *Phys. Rev. B* **6**, 4370–4379 (1972).

## Methods

**Numerical Calculations.** All numerical simulations were done using COMSOL Multiphysics version 5.6.

The model is composed of a rectangular volume with a square footprint with sides  $A = 250$  nm and periodic boundary conditions were employed for both  $u$  and  $v$  directions. The DWP unit cell is divided into two parts of air and glass, with one gold nanobrick placed against the glass region. The corners of the nanobrick are rounded with a 5 nm radius. The refractive index of air is set as 1 and that of glass as 1.46 for all wavelengths, while the gold permittivity was interpolated as a function of wavelength from experimental tabulated values<sup>28</sup>.

Using this model, the complex reflection and transmission coefficients for the glass/OMS/air interface are calculated for both propagation directions (i.e., normal incident from glass or air) and for light linearly polarized along both  $u$  and  $v$  separately. These are used to calculate the total reflection coefficient  $r_{\text{FP}}$  by including the gold substrate with the FP equation<sup>22–24</sup>

$$r_{\text{FP}} = r_{12} + \frac{t_{12}t_{21}r_{23}e^{izkn_2T_a}}{1-r_{12}r_{23}e^{izkn_2T_a}} \quad (1)$$

Here,  $r_{mn}$  ( $t_{mn}$ ) denotes the reflection (transmission) coefficients for light incident on material  $n$  from material  $m$  and the materials are numbered 1, 2, 3 for respectively glass substrate, air and gold substrate, and  $k$  is the wavenumber in air. Note that the effect of the OMS on the interface between the air and glass substrate is included in  $r_{12}$ ,  $t_{12}$  and  $t_{21}$ , and that even for normal incidence  $r_{\text{FP}}$  are polarization-dependent due to the anisotropy of the OMS layer. The reflection coefficient  $r_{23}$  from the air/gold interface is calculated directly using Fresnel equation. An illustration of the DWP geometry is shown in Supplementary Fig. S2 together with plots explaining the behavior of the total reflection coefficient  $r_{\text{FP}}$  with varying  $T_a$ .

For air gaps much smaller than the wavelengths, there is near-field coupling between the nanobricks and the gold substrate in addition to the FP resonances<sup>10,23</sup>, requiring numerical simulations including also the gold substrate in COMSOL. The results obtained using FP equation were confirmed to give the same results as COMSOL simulations with the whole glass/nanobrick/air/gold substrate model when  $T_a > 100$  nm for a wavelength of  $\lambda = 800$  nm.

As a final comment, to compare with the measurements, the imaginary part of the gold permittivity is increased by three times in the simulations of Figs. 2, 4 and Supplementary Figs. S5-S13, accounting for the surface roughness and grain boundary effects of the fabricated gold nanobricks as well as the increased damping associated with the titanium (Ti) adhesion layers between gold/glass interface.

**Fabrication.** The OMS for developing MEMS-OMS DWP were fabricated using electron beam lithography (EBL), thin-film deposition, and lift-off techniques. First, a 100-nm-thick poly(methyl methacrylate) (PMMA A2, MicroChem) layer and a 40-nm thick conductive polymer layer (AR-PC 5090, Allresist) were successively spin-coated on the glass substrate (Borofloat 33 wafer, Wafer Universe). Note that the glass

substrate was preprocessed to have a 10- $\mu\text{m}$ -high circular pedestal using optical lithography and wet etching, and the OMS pattern was defined on the pedestal using EBL (JEOL JSM-6500F field-emission SEM with a Raith Elphy Quantum lithography system). After development, the OMS layer was formulated by depositing a 1-nm Ti adhesion layer and a 50-nm gold layer (Tornado 400, Cryofox) followed by lift-off in acetone (Supplementary Fig. S4). The pedestal on the glass substrate is very effective for reducing the possible contaminants between the MEMS mirror and OMS surface, thus improving the stability and repeatability of the DWP components. The MEMS mirror is fabricated using standard semiconductor manufacturing processes (Supplementary Fig. S3), in which thin-film lead zirconate titanate (PZT) is incorporated for long-stroke, low-voltage electrical actuation. For use in the MEMS-OMS component, the ultra-flat MEMS mirror was sputtered with a 100 nm gold layer. After the gold deposition, the MEMS mirror surface is inspected with a white light interferometry (Zygo NewView 6300), showing overall good flatness and roughness all over the whole MEMS mirror (i.e.,  $\sim 3$  mm diameter) (Supplementary Fig. S3).

The MEM-OMS-based DWP component (Supplementary Fig. S4) was assembled by gluing the MEMS mirror with the glass substrate upon which OMS is structured, and then glued to a printed circuit board (PCB), followed by gold wire bonding process between the MEMS mirror and PCB for enabling simple electrical connection to a voltage controller used to actuate the MEMS mirror.

**Characterization.** The experimental set is shown in Supplementary Fig. S8. A collimated fiber-coupled supercontinuum laser (SuperK Extreme, NKT) was directed through a HWP (AHWP10M-980, Thorlabs), a mirror, a linear polarizer ( $\text{Pol}_1$ ; LPNIR050-MP2, Thorlabs), two beam splitters ( $\text{BS}_{1,2}$ ; CCM1-BS014, Thorlabs) successively, and then focused onto the DWP samples by an objective (Obj; M Plan Apo,  $\times 20/0.42\text{NA}$ , Mitutoyo). The combination of HWP and  $\text{Pol}_1$  is used for altering the input LP states as well as the intensity. The reflected light was collected by the same objective and passing through two beam splitters ( $\text{BS}_{2,3}$ ; CCM1-BS014, Thorlabs) and a tube lens (TL; TTL200-S8, Thorlabs), generating the first direct image plane where an iris is placed for filtering out the reflection light within the DWP area. The first direct image is then transformed by a relay lens (RL; AC254-200-B-ML,  $f = 200$  mm, Thorlabs) to the corresponding Fourier image and captured by a CCD camera (CCD; DCC1545M, Thorlabs), according to a

2f configuration. Note that a flip lens (FL; AC254-100-B-ML,  $f = 100$  mm, Thorlabs) is used for switching between the direct and Fourier images, and Stokes analyzer composed of a QWP (AQWP10M-980, Thorlabs) and a linear polarizer (Pol<sub>2</sub>; LPNIR050-MP2, Thorlabs) is implemented before the CCD camera for performing full Stokes polarimetry<sup>25</sup>. Two beam splitters are configured for cross-compensating the polarization-dependent phase-shifts in the beam splitters for both incidence and reflection routes.

To obtain the wavelength-resolved full Stokes parameters, we replaced the CCD camera with a fiber-coupled spectrometer (QE *Pro*, Ocean Optics) and conducted measurements at the Fourier image plane. By rotating the QWP and Pol<sub>2</sub>, we recorded polarization-resolved spectra of  $I_x(\lambda)$ ,  $I_y(\lambda)$ ,  $I_a(\lambda)$ ,  $I_b(\lambda)$ ,  $I_r(\lambda)$ ,  $I_l(\lambda)$ , and the Stokes parameters ( $s_1, s_2, s_3$ ) are calculated as  $s_1 = (I_x(\lambda) - I_y(\lambda)) / (I_x(\lambda) + I_y(\lambda))$ ,  $s_2 = (I_a(\lambda) - I_b(\lambda)) / (I_x(\lambda) + I_y(\lambda))$ ,  $s_3 = (I_r(\lambda) - I_l(\lambda)) / (I_x(\lambda) + I_y(\lambda))$ . For a reasonable comparison with the simulations, the Stokes parameters ( $s_1, s_2, s_3$ ) are normalized to the polarized proportion of the reflected light beam:  $S_{1,2,3} = \frac{s_{1,2,3}}{\text{DOP}}$ , and the degree of polarization (DOP) is defined as  $\text{DOP} = \sqrt{s_1^2 + s_2^2 + s_3^2}$ .

The coordinates system used is indicated in the lower-left inset of Fig. 1a, with  $z$  being the optical axis,  $x$  and  $y$  are transverse axes in the laboratory frame of reference, while  $u$  and  $v$  are transverse axes oriented along the sides of the rectangular nanobricks. The angle between  $u$  and  $x$  is denoted  $\theta_{\text{DWP}}$ , while the angle between the  $x$  axis and polarization direction of LP incident light is denoted  $\theta_{\text{LP}}$ .

To estimate the switching speeds between different orthogonal LP and CP bases (i.e., different DWP status), the setup described above is modified by replacing the input laser and CCD camera with a *cw* Ti:sapphire laser (Spectra-Physics 3900S, wavelength range: 700 to 1000 nm), and a photodetector (PD; PDA20CS-EC, Thorlabs), respectively. The signals from the PD are acquired with an oscilloscope (DSOX2024A, Keysight). In the measurement, the MEMS-OMS-based DWP is actuated with periodically alternating voltages and different polarizations (i.e.,  $|x\rangle$ ,  $|y\rangle$ ,  $|r\rangle$  and  $|l\rangle$ ) can be filtered by the Stokes analyzer.

## **Acknowledgements**

This research has received funding from the VKR Foundation (Award in Technical and Natural Sciences 2019 and Grant No. 37372); the EU Horizon 2020 research and innovation programme (Marie Skłodowska-Curie grant agreement No. 713694); as well as from the Research Council of Norway under project number 323322. C. M. acknowledges Yao Xiao for the help in figure preparation, Ying Qu and Martin Thomaschewski for their help in the experiments. P.T. acknowledges Jon Vedum for helping with the control electronics for the MEMS mirrors.

## **Author contributions**

P. T. and C. M. performed the simulations and designed the OMS, fabricated and assembled the MEMS-OMS-based DWP samples. C. M. constructed the experimental set up, performed the measurements and analysed the data. All authors contributed to the project idea, discussion of the results obtained and writing of the manuscript. S. I. B. supervised the project.

## Figures and Captions

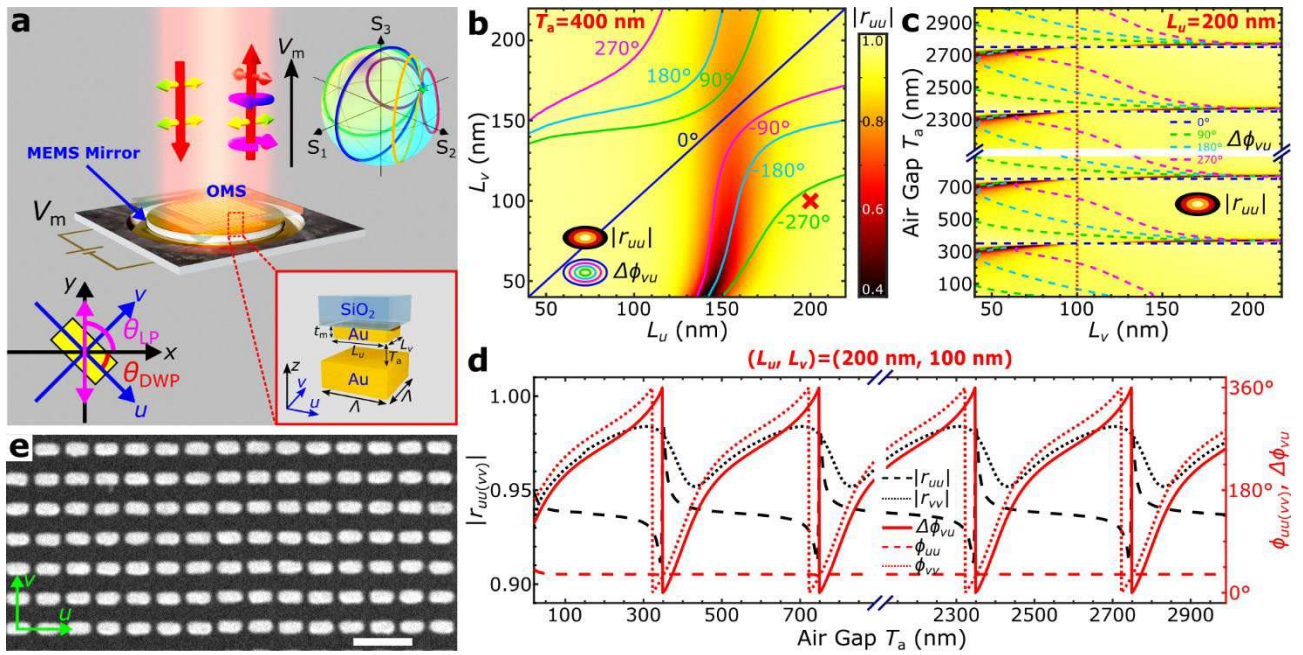


**Fig. 1 | Electrically controlled MEMS-OMS-based DWP.** **a**, Schematic of the DWP component consisting of an OMS on a glass substrate, mounted on a movable MEMS mirror. By applying a voltage  $V_m$ , the separation between the MEMS mirror and OMS can be changed, thereby achieving a continuously variable birefringence in reflection. The bottom-right inset is a close-up view of the MEMS-OMS unit cell representing a gold nanobrick on glass separated by an air gap  $T_a$  from the MEMS gold mirror. The top-right inset illustrates, with the Poincaré sphere, different reflected field polarization trajectories that can be realized by changing  $V_m$  for the fixed incident LP state  $|y\rangle$  ( $\theta_{LP} = 90^\circ$ ) and 5 different DWP orientations ( $\theta_{DWP} = 15^\circ, 30^\circ, 45^\circ, 60^\circ, 75^\circ$ ). The coordinate systems used are shown in the bottom-left inset. **b**, Reflection amplitude ( $|r_{uu}|$ ) and birefringence ( $\Delta\phi_{vu}$ ) calculated as a function of the nanobrick side lengths  $L_u$  and  $L_v$ , for the air gap  $T_a = 400$  nm, with other parameters as follows:  $\lambda = 800$  nm,  $t_m = 50$  nm,  $A = 250$  nm. Colour map is related to the reflection amplitude, while coloured lines represent constant birefringence contours. The red cross indicates the selected nanobrick dimensions  $L_u \times L_v = 200$  nm  $\times$  100 nm. **c**, Reflection amplitude ( $|r_{uu}|$ ) and birefringence ( $\Delta\phi_{vu}$ ) calculated as a function of the nanobrick side length  $L_v$  and air gap  $T_a$ , for the other side length  $L_u = 200$  nm. Colour map is related to the reflection amplitude, while coloured dashed lines represent constant birefringence contours. The vertical, red dotted line corresponds to the selected nanobrick

dimensions  $L_u \times L_v = 200 \text{ nm} \times 100 \text{ nm}$ . **d**, Reflection amplitudes  $|r_{uu(vv)}|$  (black dashed and dotted), phase  $\phi_{uu(vv)}$  (red dashed and dotted) and birefringence  $\Delta\phi_{vu}$  (red solid) calculated as a function of the air gap  $T_a$  for the selected nanobrick dimensions  $L_u \times L_v = 200 \text{ nm} \times 100 \text{ nm}$ . **e**, Scanning electron microscopy (SEM) image of a part of the OMS nanobrick array fabricated on the glass substrate. Scale bar is 500 nm.

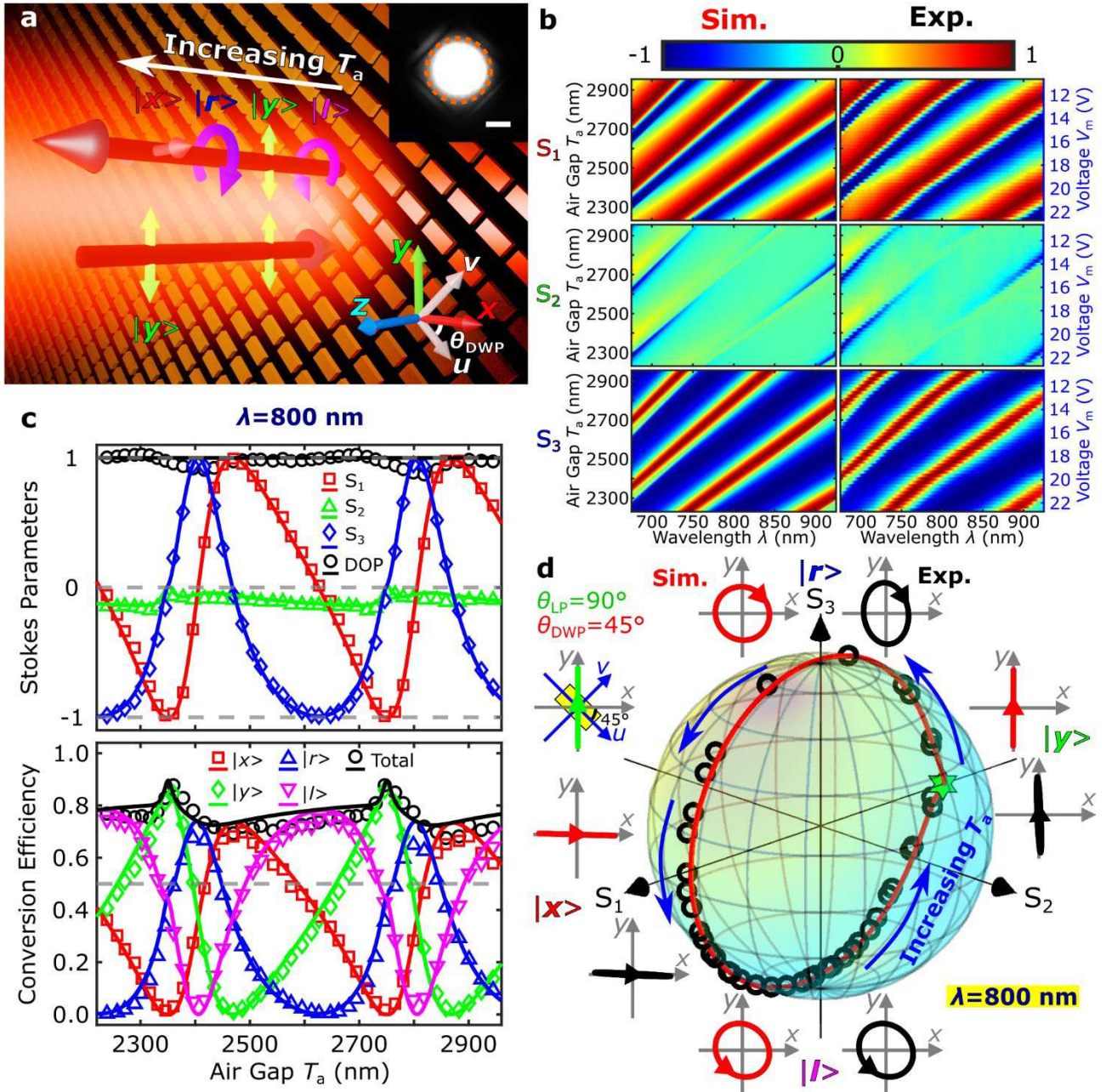


**Fig. 2 | Polarization transformations for the incident LP oriented at  $45^\circ$  with respect to the DWP axes.**

**a**, Schematic of the DWP operation at the wavelength of 800 nm for the fixed incident LP state  $|y\rangle$  ( $\theta_{LP} = 90^\circ$ ) and DWP orientation  $\theta_{DWP} = 45^\circ$ , illustrating the reflected light polarizations being continuously changed from  $|l\rangle$ ,  $|y\rangle$ ,  $|r\rangle$  to  $|x\rangle$  with increasing the air gap  $T_a$ . The inset is a typical optical image of the OMS array illuminated with the incident laser spot confined within the orange dashed circle. Scale bar is 10  $\mu\text{m}$

$\mu\text{m}$ . **b**, Calculated (left) and measured (right) normalized Stokes parameters ( $S_1, S_2, S_3$ ) of the reflected light as a function of the air gap  $T_a$  and light wavelength  $\lambda$ . **c**, Calculated (lines) and measured (markers) normalized Stokes parameters (above) and polarization conversion efficiencies (below) as a function of the air gap  $T_a$  for the light wavelength  $\lambda = 800 \text{ nm}$ . **d**, Calculated (line) and measured (circles) polarization trajectory on the Poincaré sphere mapping the reflected light polarization evolution shown in **(c)**. As the air gap  $T_a$  increases, the reflected polarization state revolves repeatedly around the sphere. The green star marks the incident LP state:  $|y\rangle$ . The calculated (red) and measured (black) polarization ellipses illustrate the polarization contrast between the main orthogonal polarization states ( $|x\rangle$  and  $|y\rangle$ ,  $|r\rangle$  and  $|l\rangle$ ) realized by tuning the air gap  $T_a$ .

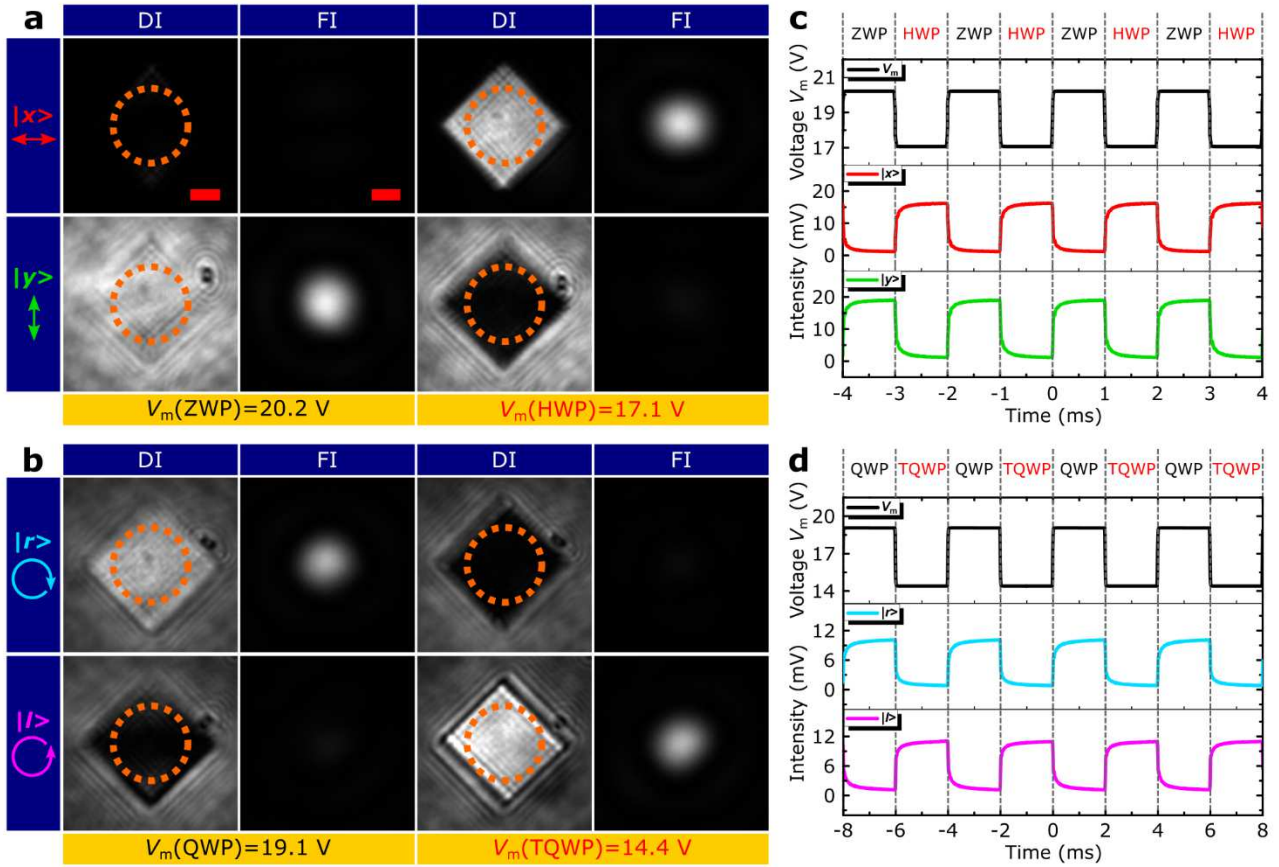


**Fig. 3 | Polarization conversion dynamics.** **a-b**, Optical images of the reflected light at the direct image (DI) and Fourier image (FI) planes for the fixed input LP state  $|y\rangle$  ( $\theta_{\text{LP}} = 90^\circ$ ) and DWP orientation ( $\theta_{\text{DWP}} = 45^\circ$ ) at  $\lambda = 800\text{ nm}$ , showing polarization modulation between orthogonal **(a)** LP states ( $|x\rangle$ ,  $|y\rangle$ ), corresponding to ZWP/HWP transformation, by changing the actuation voltage  $V_m$  from 20.2 to 17.1 V, and **(b)** CP states ( $|r\rangle$ ,  $|l\rangle$ ), corresponding to QWP/TQWP transformation, by changing the actuation voltage  $V_m$  from 19.1 to 14.4 V. For the FI images, the light is filtered using an iris letting through only light reflected from inside the orange dashed circles (shown in DIs). The leftmost column in **(a, b)** indicates the polarizer orientations used for filtering the respective polarization states in the reflected light. Scale bars in the DIs and FIs are  $10\ \mu\text{m}$  and  $0.02k_0$ , respectively. **c-d**, Temporal evolution of the reflected light power for **(c)** ZWP/HWP and **(d)** QWP/TQWP transformations, measured by actuating the MEMS mirror with a periodic rectangular signal and filtering respective polarization states.

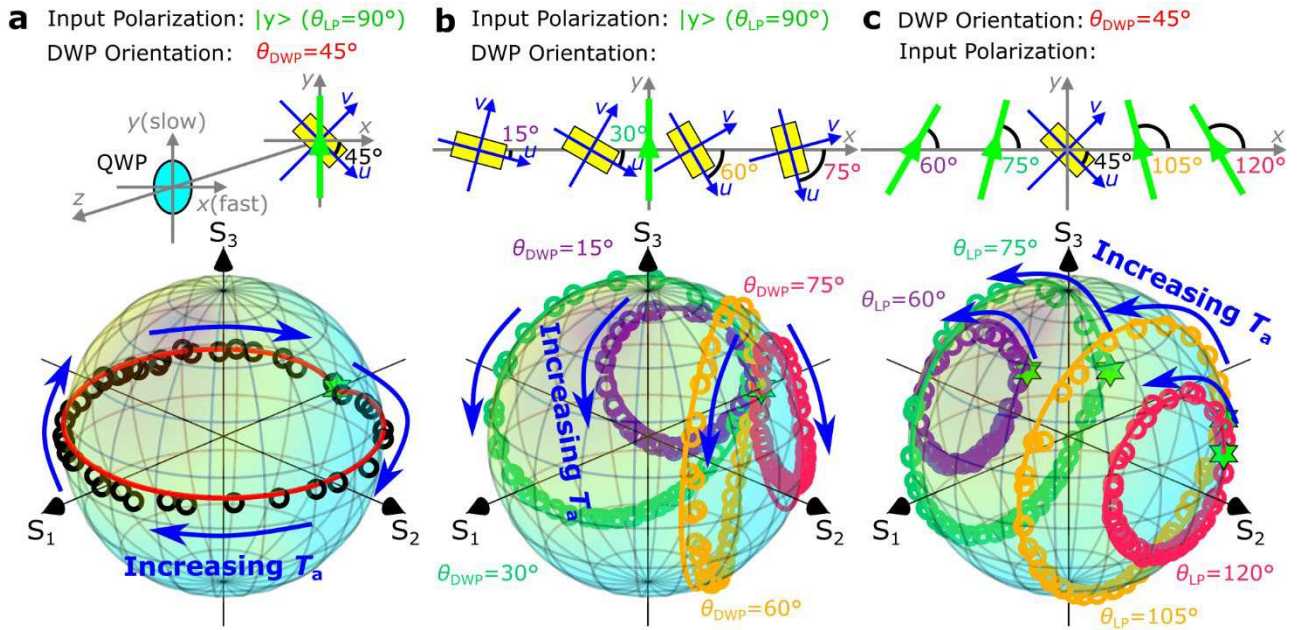


**Fig. 4 | Versatile polarization transformations.** **a-c**, Calculated (lines) and measured (circles) polarization trajectories on the Poincaré sphere realized at the wavelength of 800 nm by tuning the air gap  $T_a$  for different DWP orientations, illustrating the diversity of possible polarization transformations: **(a)** continuous LP rotation realized by combining the DWP with a conventional QWP with the incident LP state  $|y\rangle$  and DWP orientation  $\theta_{DWP} = 45^\circ$ , **(b)** various elliptical polarization transformations realized for different DWP orientations with the fixed incident LP state  $|y\rangle$ , and **(c)** various elliptical polarization transformations realized for different incident LP states with the fixed DWP orientation  $\theta_{DWP} = 45^\circ$ . The green stars in **(a-c)** indicate respective incident LP states.

## Supplementary Files

This is a list of supplementary files associated with this preprint. Click to download.

- [DWPSupplementary.pdf](#)
- [VideoS1.mp4](#)
- [VideoS2.mp4](#)
- [VideoS3.mp4](#)
- [VideoS4.mp4](#)
- [VideoS5.mp4](#)
- [VideoS6.mp4](#)